Nanoscale

Accepted Manuscript

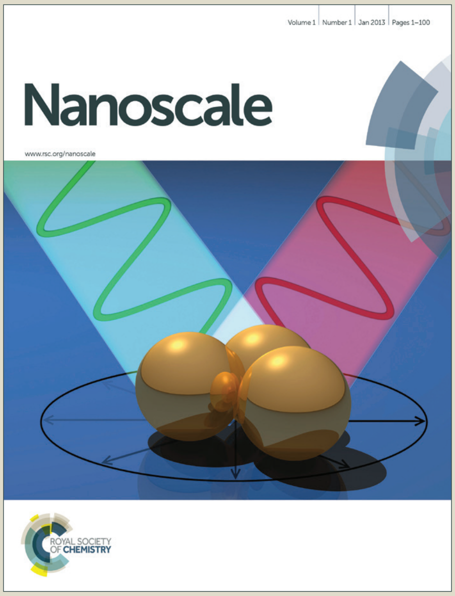

ROYAL SOCIETY OF CHEMISTRY

www.rsc.org/nanoscale

Manuscript ID: NR-ART-10-2013-005456.R3

Title: Tailoring Conduction Band of Titanium Oxide by Doping Tungsten for Efficient Electron Injection in Sensitized Photoanode

Authors: Alexander M. Cant, Fuzhi Huang, Xiao Li Zhang, Yang Chen, Yi-Bing Cheng, Rose Amal

Colour graphic:

The combination of finely tuned chemical and optical properties of the photoanode material enabled a further enhancement on the dye-sensitized solar cell performance.

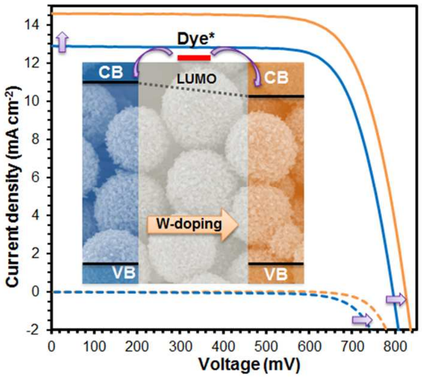

Journal Name RSCPublishing

ARTICLE

Cite this: DOI: 10.1039/x0xx00000x

Received 00th January 2012,
Accepted 00th January 2012

DOI: 10.1039/x0xx00000x

www.rsc.org/

Tailoring Conduction Band of Titanium Oxide by Doping Tungsten for Efficient Electron Injection in Sensitized Photoanode

Alex M. Cant,[a] Fuzhi Huang,[b] Xiao Li Zhang,[a,]* Yang Chen,[b] Yi-Bing Cheng[b] and Rose Amal[a]

Aiming to overcome the current limits for dye-sensitized solar cells (DSSC) to reach a higher solar energy conversion efficiency, this work set out to investigate the feasibility of combining a variety of preparation techniques that can finely tailor the optical and electrochemical properties of the photoanode material. The obtained tungsten doped mesoporous titania spheres exhibited significant enhancements on photocurrent and open-circuit voltage leading to an over 15% increase on cell efficiency. With a single layer 12 μm film, the W-doped photoanode reached a solar energy conversion efficiency of 8.9% which is far greater than a 5.7% efficiency obtained by photoanode film prepared from Degussa P25 TiO_2 nanoparticles. This was greatly attributed to the superior light scattering effect from the mesostructure and the increased electron injection drive-force from the down-shifted conduction band after doping.

Introduction

Dye-sensitized solar cells (DSSCs), a relatively young technology, offers a potential solution to poor solar cost efficiency with the advantages of low materials costs, simpler manufacture process, desired durability, and a larger range of potential outdoor and indoor applications [1,2]. As an essential component of DSSC operation, semiconducting charge collector provides a mechanism for sensitizer molecules to release electrons which are passed through to the external circuit of the cell. The most widely adopted and effective charge collecting material to date is titanium dioxide, possessing a conduction band level in the ideal range and an excellent chemical stability.

The energy variation between the lowest unoccupied molecular orbital (LUMO) of the sensitizer and the conduction band edge of TiO_2 works as a driving force for the electron injection from excited dye to the photoanode film [3,4]. The conduction band of titanium dioxide is slightly higher than the ideal value resulting in an unfavourable smaller energy variation to the LUMO. This prevents the DSSC reaching a high incident photon-to-current conversion efficiency (IPCE) due to the dramatic electron loses in back reactions (recombination). Control over the conduction band of TiO_2 through chemical and structural changes of the crystalline titanium dioxide has yet been fully explored to provide a sufficient driving force for electron injection.

Modification of semiconductors with the dopants that have equivalent ionic radii to the cation or the negion has proven ability of finely tuning the chemical and optical properties, as well as the conduction band edge of the semiconductors [5-9]. The most prevalent potential dopants for titanium oxide with these radii include zinc (II; 74 pm), magnesium (II; 72 pm), aluminium (III; 53.5 pm), tin (IV; 69 pm), niobium (V; 64 pm), tantalum (V; 64 pm), vanadium (V; 54 pm) and tungsten (VI; 60 pm) [10]. The closest radii value to that of titanium (IV) ion (60.5 pm) makes tungsten (VI) ion an ideal dopant for minimized crystal defects increase following the conduction band edge change [11]. To date, only few literatures have reported the use of tungsten doped titanium oxide nanoparticles as photoanode material with clear improvement on the photocurrent attributed to the positively shifted conduction band. It was reported that the interaction between the oxygen vacancies and the W-dopant greatly contributes to resemble the conduction band minimum of TiO_2 [12]. The preparation involved the use of unfavourable insoluble tungstic acid (H_2WO_4) as W-dopant resource and tedious multistep procedure [11, 13]. Using water soluble tungsten resources instead would simplify the preparation and prevent negative issues such as the occurrences of inhomogeneously dispersed dopant or small WO_3 clusters in the doping-body – titanium dioxide; such preparation approach has yet been explored.

Additionally, recent researches of morphology controlled syntheses for the charge collecting materials, titanium dioxide in particular, with desired porosity, crystallinity and optical property have succeeded in significantly enhancing the light harvesting capacity of the sensitized photoanodes [14-18]. Combining the well-controlled morphology with finely-tailed chemical properties for multiple gains in light harvesting and efficient electron injection and transfer is highly expected to further lift DSSCs performance; and has yet been considered so far. Herein, the present work used a stable and water-soluble precursor to synthesize highly crystalline W-doped TiO_2 (anatase) mesoporous spheres through a simple hydrothermal reaction process. The water-soluble sodium tungstate enabled the combining of finely tailored chemical properties with the controlled morphology of crystalline mesoporous TiO_2 as a leveraging approach for multiple gains towards high efficiency DSSC system. When used as photoanode material, the W-doping was found to assist the electron injection and transfer which paid great tributes to the significant enhancements on overall PCE performance from 7.7% to 8.9%, an increase proportion of over 15%, standing on growths of short circuit current (J_{sc}) for over 1.5 mA/cm^2 and open circuit voltage (V_{oc}) for approximately 30 mV. While P25 nanoparticle based DSSC only gave a maximum efficiency of 5.7%.

Experimental

Materials synthesis

All chemicals including titanium butoxide (97%, Sigma Aldrich), sodium tungstate dihydrate (Sigma Aldrich), acetonitrile (Ajex Fine Chemical), butan-1-ol (Ajex Fine Chemical), ethanol (Ajex Fine Chemical) and ammonia (28%, Ajex Fine Chemical) used are reagent grade unless stated otherwise. The synthesis of spherical mesoporous titanium dioxide nanoparticle aggregates was based on the modification of the approach demonstrated in our previous report [18]. Titanium butoxide (7.16 mL) was added to 200 mL of a 50:50 solvent mixture of acetonitrile and butan-1-ol, while under moderate stir. To a second solution containing the same solvent mixture, distilled water (3.6 mL) and ammonia (2.7 mL) was added to the titanium butoxide mixture quickly, forming a white precipitate, while stirring speed was maintained. The solution was then left to stir for 2 hours.

The white precipitate was collected, and then washed three times with ethanol. The white precursor spheres were then dispersed in 30 mL of solvent mixture containing absolute ethanol (20 mL), distilled water (10 mL) and 0.5 mL ammonia. The solution was placed in a Teflon-lined autoclaved and heated at 160°C for 16 hours. Following solvothermal treatment the powder was then washed with ethanol, acetone and dried at room temperature.

Tungsten doping solution was prepared by dissolving sodium tungstate dihydrate (0.52 g) in distilled water (50 mL). Prior to addition the stock solution was moderately stirred and sonicated. The solution was then used in place of water added to the solvent mixture prior to solvothermal treatment, according to the necessary doping level. Doping of tungsten was performed on a W/Ti atomic bases at 0 % (0 mL stock solution, sample **W0**), 0.07 % (0.421 mL stock solution, sample **W1**) and 0.13 % (0.842 mL stock solution, sample **W2**). Smaples with higher doping level such as 0.25 (**W3**) and 0.5 at% (**W4**) were also prepared for comparison.

Characterization

Morphologies of the products were observed by using a high resolution field emission scanning electron microscope (SEM, Hitachi S-900). Crystal phase of the products were verified on a PANalytical Xpert Multipurpose X-ray Diffraction System (MPD) with Cu Kα radiation under 40 kV working voltage. Nitrogen adsorption – desorption isotherms were measured on a Micromeritics Tristar 3000 system. Samples were degased at 100 °C on a vacuum line overnight. Specific surface areas were calculated by utilizing a standard Brunauer-Emmett-Teller (BET) method. Adsorption of the isotherms was used to provide pore size distributions. UV-vis reflectance spectra of the powder samples were measured on a Shimadzu UV3600 UV-vis-NIR spectrometer. PerkinElmer quadrapole Nexion ICPMS integrated with an ESI-NewWave NWR213 Laser Ablation accessory (LA-ICPMS) was used to quantitative analysis of the chemical compositions of W-doped TiO_2.

Dye-sensitized solar cell construction

The samples (2.0 g) were dispersed in absolute ethanol (40 mL) and sonicated for 30 min. Ethyl cellulose (1.0 g) and terpinol (8.0 g) were added to the solution and finely dispersed by sonication and stirring before evaporated at 40 °C to a paste. A thin blocking layer of TiO_2 were prepared on FTO glass (Nippon, 10 Ω/square) by spray pyrolysis of 7.5% w/w solution of titanium isopropoxide bisacetylacetonate in ethanol at 450 °C. Photoanode films with thickness of approximately 12 μm (4×4 mm^2) were printed onto FTO glass by using a screen printer. The films were sintered in air as follows: 150 °C for 10 min, 325 °C for 5 min, 375 °C for 5 min, 450 °C for 30 min, and finally 500 °C for 15 min. These films were re-sintered for 30 min at 450 °C before sensitized in a 0.3 mM commercial N719 (Dyesol) solution overnight.

Counter electrode were prepared by thermally decomposing H_2PtCl_6 (10 mM in ethanol) on FTO glass. Sandwich cells were assembled by sealing the photoanode onto the Pt counter electrode with a 25 μm thick Surlyn (8×8 mm^2). The electrolyte, containing 0.03 M iodine, 0.5 M 4-terbutylpyridine, 0.6 M 1-butyl-3-methylimidazolium iodide, and 0.1 M guanidinium thiocyanate in a mixed acetonitrile/valeronitrile (V/V = 17 : 3) solution, was introduced into the cell via a vacuum filling method.

The thickness of the electrode films was measured by a profilometer (DEKTAK 150, Veeco Instruments Inc). The sealed solar cells were shielded by a black metal mask with an aperture area of 6×6 mm^2, and measured the photovoltaic properties using a Keithley 2400 Source Meter under the irradiation of simulated sunlight (100 mW/cm^2) provided by an Oriel solar simulator with an AM 1.5 filter. IPCE plotted as a function of excitation wavelength was recorded on a Keithley 2400 Source Meter under the irradiation of a 300 W xenon lamp with an Oriel Cornerstone^{TM} 2601/4m monochromator. Electrochemical impedance spectra (EIS), measured with an AutoLab PST A30 in a frequency range of 0.1 – 10^5 Hz under 1 sun irradiation with an applied bias of V_{oc}.

Results and discussion

Spherical hybrid titanium oxide precursors used in this work were synthesized through a sol-gel approach [18]. The overall morphology of the hybrid precursor spheres was reviewed by field emission scanning electron microscope (SEM) imaging technology in Figure S1, supplementary information. The untreated precursor spheres are of poly-dispersion with a main diameter range of 400 – 800 nm. The precursor spheres have apparently smooth surface with no defined crystallites. Corresponding X-ray diffraction (XRD) analysis in Figure S1 further confirmed the amorphous structure of the hybrid precursor spheres as no diffraction peak can be found.

A facile one-pot hydrothermal approach to produce W-doped TiO_2 spheres without changing the mesoporous texture was established in the present work involving the directly mixing sodium tungstate in the hydrothermal solvent with the precursor spheres. Following the hydrothermal treatment at 160 °C, the surfaces of the spheres became considerably rougher as can be observed in Figure 1 a). At higher magnification in

Figure 1b), the surface displays distinct rod-like nanoparticles of approximately 15 - 20 nm in diameter and length of up to approximately 50 nm. Figure 1 c) to f) are of SEM observations for the W-doped TiO_2 mesoporous spheres, sample **W1** and **W2**, revealing the minor effect of the doping on mesoscope structures as both spheres and individual nanoparticles are of the similar sizes and appearances compared to the un-doped TiO_2, sample **W0**. This also suggests that tungsten would become part of the titanium dioxide lattice by replacing Ti (VI) during hydrothermal process as a result of the close ion radii of tungsten (VI; 60 pm) and titanium (V; 60.5 pm). The effect on the visual surface appearance of the TiO_2 spheres and nanoparticles from the doping are therefore small enough as negligible for SEM observations.

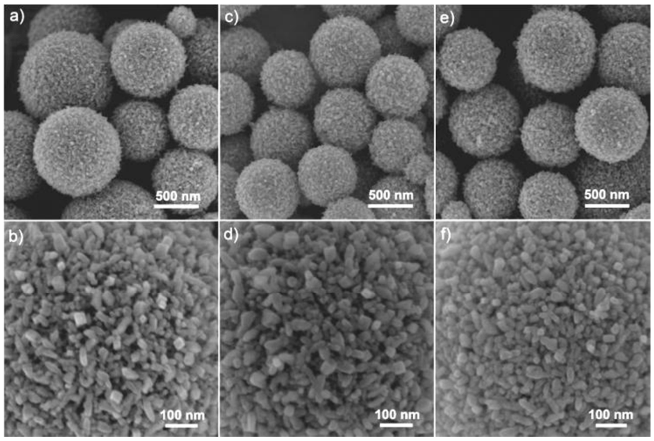

Figure 1. SEM images of non-doped and W-doped spherical mesoporous TiO_2: a) and b) sample W0; c) and d) sample W1; e) and f) sample W2.

SEM and STEM (scanning transmission electron microscopy) equipped with an energy-dispersive X-ray spectroscopy are commonly used for chemical composition analysis and element mapping that are no longer suitable for the W-doped TiO_2 in the present work as the doping levels are below 1 at% at approximately 0.07 at% for sample **W1** and 0.13 at% for sample **W2**. In contrast, laser ablation inductively coupled plasma mass spectrometry (LA-ICPMS) that is able to perform ultra-highly sensitive chemical analysis down to ppb level was employed in the present work to confirm the real doping concentration in the products. As shown in Table S1 (supplementary information), the LA-ICPMS result reveals a W/Ti mass basis of 0.26 wt% in the sample **W1** that is in a good agreement with the amount of tungsten in the reactants. The result proves the doping process with the use of water soluble sodium tungstate as W-source in a one-pot hydrothermal process is a reliable approach.

The doping effect on the crystal structure of the prepared spherical mesoporous TiO_2 were investigated using XRD analysis. In Figure 2 a), all three XRD patterns matching well with anatase phase TiO_2 (JCPDS card No.21-1272) in the absence of a second phase. Attributed to the low doping concentrations in samples **W1** and **W2** (with W/Ti atomic bases of 0.07 and 0.13 %, respectively) and the comparable ionic radii of tungsten (VI) and titanium (V), no peak shift was detected from the W-doped mesoporous TiO_2 (sample **W0**). Additionally, the XRD patterns of the samples **W1** and **W2** also have close values of peak intensity and width compared to those of the sample **W0**. The average crystallite sizes of nanoparticles in the three samples were also estimated by using Scherrer equation using diffraction peaks of (101), (004), (200) and (204) disclose almost unchanged size of the nanoparticles with W-doping and preferred crystal orientation – rod-shape nanoparticles. The XRD analyses agree well with the SEM observations and reflect the minor influence from tungsten doping on crystalline structure of titanium dioxide at such low doping levels.

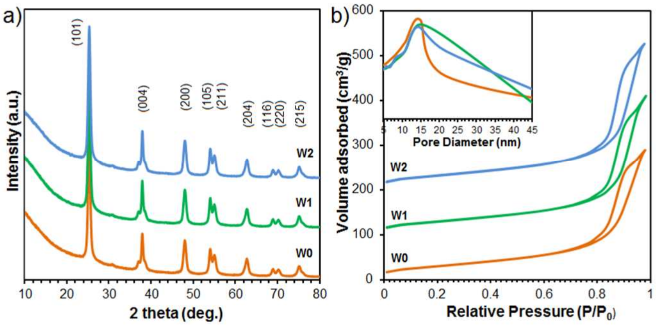

Figure 2. a) Corresponding XRD patterns and b) nitrogen sorption isotherms of non-doped and W-doped spherical mesoporous TiO_2. The XRD curves of W1 and W2 samples were shifted by 10000 and 20000 a.u.; the isotherm plots of W1 and W2 samples were shifted by 100 and 200 cm^3 g^{-1}. Inset is the corresponding pore diameter distribution.

Table 2. Corresponding physical properties – BET specific surface area (S_{BET}), pore diameter (PD) and pore volume (V_{sp}) of the non-doped and W-doped spherical mesoporous TiO_2.[a]

Sample	S_{BET} (m^2/g)	PD (nm)	V_{sp} (cm^3/g)
W0	111.4	12.8	0.45
W1	109.0	13.9	0.48
W2	117.2	13.8	0.50

Compared to nanoparticles such as Degussa P25, mesoporous TiO_2 in sub-micron size range has proven superior DSSC performance resulted from the large surface area for sensitizer adsorption, the preferable porosity to ensure an ease of access for the sensitizer molecules and the electrolyte, as well as a great light trapping effect for efficient light harvesting [17-18]. The minor influence on mesoscope structure would assist the conservation of these desired surface and optical properties. Nitrogen gas sorption was used to measure the specific surface area and porosities of the non-doped and doped mesoporous TiO_2. The isotherms and pore-size distributions are shown in Figure 2 b) and inset, and the physical properties are summarized in Table 1. In contrast to the commercial Degussa P25 nanoparticles that has a specific surface area of approximately 61.3 m^2/g (in Figure S2, supplementary information), all three mesoporous samples have type VI isotherms and featured H1 type hysteresis loops revealing a small variation of the superior specific surface areas from 109 to 117 m^2/g. The sharp capillary condensation steps at high relative pressure at P/P_0 of 0.85-0.95 suggest large pore-sizes of the samples. This is confirmed by the corresponding pore-size distribution curves with a narrow pore-size distribution centred at approximately 13 nm of mesopore structure. The nitrogen gas sorption analyses suggest that the tungsten impurity assisted a minor porosity development from 0.45 to 0.50 cm^3/g and slightly up shifted pore-size distribution centres from 12.9 to 13.9 nm. The insignificant variations of the specific surface areas and porosities between the un-doped and doped TiO_2 samples again mirror the minor influence of the dopant on the mesoscope structure of the spheres at low doping levels. To ensure the surface uptake capacities and accessibilities of the W-doped mesoporous TiO_2, dye adsorptions of the sensitized photoanode films prepared from the samples **W0**, **W1** and **W2** were further assessed. Figure S3 in supplementary information reveals negligible differences of dye adsorption for the photoanode films with undoped and doped mesoporous TiO_2.

Although it is generally accepted that band bending is negligible for small nanoparticles (such as less than 6 nm), the mesoporous TiO_2 spheres in the present work were formed by hundreds of nanoparticles with an average crystallite size over 15 nm based on SEM observation and XRD estimation which are likely to have band bending phenomena [11]. The flat-band potential (V_{fb}) of the un-doped and W-doped mesoporous TiO_2 photoanodes were assessed by Mott-Schottky analyses. In Figure 3, clear positive shifts can be observed from samples **W1** and **W2** corresponding to the downwards movements of the Fermi level with increasing the W-doping level from 0.07 to 0.13 at%. The band gap down-shifts from the un-doped to the W-doped photoanode materials were again witnessed by UV-vis absorbance spectra as displayed in Figure S4 (supplementary information), which was calculated from diffuse reflectance analyses using the Kubelka – Munk equation. The doping induced oxygen vacancy play an important role in band gap narrowing [19], which is expected to enlarge the energy variation between the conduction band of the photoanode material to the LUMO of the sensitizer. This will provide an enhanced driving force for electron injection and transport as well as suppressing the recombination in DSSC applications.

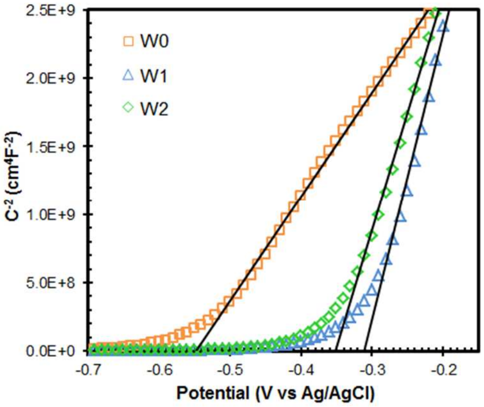

Figure 3. Mott-Schottky plots of non-doped and W-doped spherical mesoporous TiO_2.

Photoanode electrodes were prepared from samples **W0**, **W1** and **W2**, and sensitized with commercial N719 to investigate the doping influence on photovoltaic performance through the characterization of the photocurrent densities – the open circuit voltages ($J - V$) at simulated 1.5 AM 1000 W/m^2 sunlight, as shown in Figure 4 a) and summarized in Table 2. With the film thickness of approximately 12 μm, the un-doped mesoporous TiO_2 (sample **W0**) gave an overall PCE of 7.7% standing on an open circuit voltage (V_{oc}) of 795 mV and a short-circuit current density (J_{sc}) of 12.9 mA/cm^2. As expected, the W-doped mesoporous TiO_2 show significantly improved V_{oc} and J_{sc} when compared to the photoanode prepared from the sample **W0**. As a result from the superior J_{sc} of up to 14.6 mA/cm^2 and V_{oc} of 821 mV, the sample **W2** was succeeded in enhancing the overall PCE from 7.7 to 8.9%. With same dye absorption capacities, the clearly developed J_{sc} can be strongly attributed to the improved electron injection and transfer efficiencies due to the sufficient electron injection driving force resulted from the positively shifted conduction band with W-doping. The noteworthy positive shifts of dark current with increased W-doping concentration indicate greatly improved quantum efficiencies that are mainly credit for the recombination slowdown. This suggests that the down-shifted conduction band also retarded the recombination and subsidize the voltage lose from W-doping and well explains the V_{oc} increases in W-doped photoanodes. Further increasing W-doping level to 0.25 (**W3**) and 0.5 at% (**W4**) did not improve the DSSCs performances. With sample **W3**, the DSSCs gave a similar overall PCE of 9.0 % while **W4** only presented a PCE of 8.2% with clearly downgraded V_{oc} values when compared to that of **W2** photoanodes. The corresponding current – voltage curves of sensitized **W3** and **W4** photoanodes can be found in Figure S6 in supplementary information. It can be explained as the further downshifted conduction band gave a negative impact on the V_{oc}. For comparison, sensitized phoaoande films were also prepared using Degussa P25 TiO_2 nanoparticle and only provided an efficiency of 5.7%. This is majorly due to the poor J_{sc} performance of approximately 9.5 mA/cm^2 attributed to the low specific surface area and poor light scattering effect of the nanoparticles.

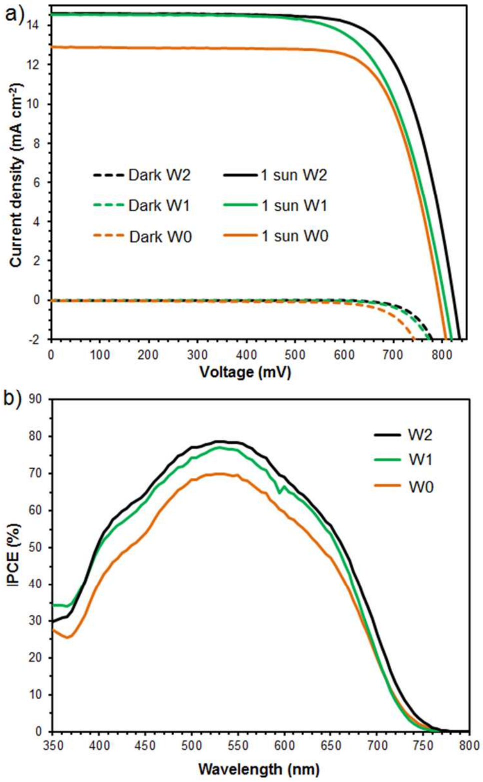

Figure 4. a) Current – voltage curves and b) IPCE of sensitized photoanodes based on non-doped and W-doped spherical mesoporous TiO_2.

Figure 4 b) displays the incident photo-to-electron conversion efficiency (IPCE) of the un-doped and W-doped titanium dioxide DSSCs. The **W0** photoanode has an IPCE of 70% at 530 nm while the W-doped TiO_2 give a maximum IPCE of 78.7%. The superior DSSC performance of the W-doped mesoporous TiO_2 witnesses the improved electron injection and transport efficiencies. This again suggests the positively shifted conduction band from the W (VI)-doping enlarges the energy difference between the LUMO of the dye molecular and the conduction band edge of photoanode material that provides a relatively sufficient driving force for rapid electron injection when compared to the un-doped TiO_2. The comparison of IPCE and normalized IPCE in Figure S5 (supplementary information) reveals the significantly enhanced light harvesting of W-doped TiO_2 mesoporous spheres over P25 nanoparticles especially in 550 – 780 nm range resulted from improved electron injection and higher diffusion reflectance capacity.

Table 2. Photovoltaic performances recorded at AM 1.5 simulated sunlight for the average of eight sensitized photoanodes, c.a. 12 μm, prepared from non-doped and W-doped spherical mesoporous TiO_2, as well as P25 TiO_2 nanoparticles.

Sample	V_{oc} (mV)	J_{sc} (mA/cm^2)	FF	Efficiency
W0	795	12.9	0.74	7.7 %
W1	804	14.4	0.73	8.2 %
W2	821	14.6	0.74	8.9 %
W3	789	15.4	0.74	9.0 %
W4	771	14.6	0.72	8.2%
P25	850	9.2	0.73	5.7%

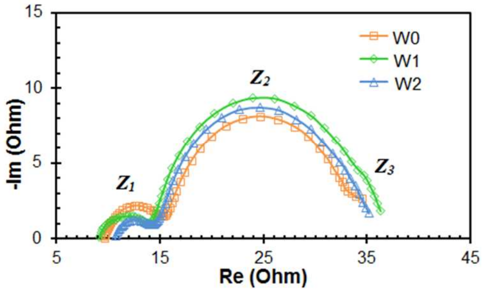

Figure 5. Impedance spectra of DSCs based on non-doped and W-doped spherical mesoporous TiO_2.

Electrochemical impedance spectroscopy (EIS) is a proven analytical technique for kinetic processes in DSSCs and was used in the present work to study the W-doping effect on the charge transport properties of the photoelectrode films [20-24]. Figure 4 displays the corresponding EIS Nyquist plots of the DSSCs prepared from samples **W0**, **W1** and **W2**. The Nyquist plots have three typical arcs allocated to the charge transfer processes at the interface of Pt/electrolyte (Z_1), the interface of TiO_2/dye/electrolyte (Z_2), and the Nernst diffusion within the electrolyte (Z_3), respectively. The electron transport resistance of the three devices, 4.0Ω, 1.7Ω, and 1.3Ω for W0, W1, and W2, respectively, were extracted from the Nyquist plots by fitting with software ZView. The electron conductivity in the mesoporous photoanodes was improved with the increased W-doping. The W (VI) dopant substitute Ti (IV) in anatase TiO_2 works as a high charge state doping that one dopant release two free electrons leading to high electron mobility and thus enhancing material conductivity [25]. Despite the application of very small doping amounts of the W(VI) in the present work, significant resistance decreases were observed. The medium frequency arc Z_2 corresponds to the electron transport at the interface of TiO_2/dye/electrolyte. The charge transfer resistance (R_{ct}) demonstrating the electron-hole recombination can be therefore calculated from the diameter of medium frequency arc Z_2. The R_{ct} values of the DSSCs rises following the increase of W-dopant proportion suggesting a retarded recombination in DSSC prepared from **W1** and **W2**. The promoted charge transport and suppressed recombination, therefore, acted as compensation and overturned the V_{oc} lose from the downshifted conduction band from W-doping. This led to both enhanced J_{sc} and V_{oc} as observed in the DSSCs prepared from W-doped samples **W1** and **W2.**

Conclusions

In conclusion, W-doped mesoporous TiO_2 submicron spheres size range 400 – 800 nm obtained from the aggregation of 15-20 nm nanoparticles were successfully synthesized through a sol-gel combined hydrothermal process. The utilization of water soluble sodium tungstate as W-doping source enabled a stoichiometric doping approach as witnessed by LA-ICPMS analysis result. The positively shifted conduction band from the W-doping assisted the electron injection and transfer in DSSC devices which resulted in greatly improved photocurrent and voltage and contributed to an over 15% increased cell efficiency. The doping influence on conduction band, electron injection and transfer were confirmed by Mott-Schottky analyses, UV-vis absorbance spectra and EIS studies.

Acknowledgements

The authors would like to thank the Australian Research Council providing financial support. Dr X. L. Zhang greatly appreciates the University of New South Wales (UNSW) for providing a Vice-Chancellor's Research Fellow and fellowship extension with funding support. The authors acknowledge the use of facilities in the Electron Microscope Unit at UNSW.

Notes and references

[a] ARC Centre of Excellence for Functional Nanomaterials, School of Chemical Engineering, The University of New South Wales, Kensington, Sydney 2052, Australia. Corresponding author Email: xiaolizhang.z@gmail.com.

[b] Department of Materials Engineering, Monash University, Clayton, Melbourne 3800, Australia.

† The authors contributed equally to this work.

Electronic Supplementary Information (ESI) available: [details of any supplementary information available should be included here]. See DOI: 10.1039/b000000x/

1. B. O'Regan, M. Grätzel, *Nature*, **1991**, *353*, 737.
2. Meyer, G.J., *Acs Nano*, **2010**. *4*,4337-4343.
3. A. Hagfeldt, G. Boschloo, L. Sun, L. Kloo, H. Pettersson, *Chem. Rev.,* 2010, **110**, 6595.
4. F. Odobel, L. L. Pleux, Y. Pellegrin, E. Blart, *Acc. Chem. Res.*, 2010, **43**, 1063.
5. X. Lü, X. Mou, J. Wu, D. Zhang, L. Zhang, F. Huang, F. Xu, S. Huang, *Adv. Funct. Mater.,* **2010**, *20*, 509.
6. F. Huang, Q. Li, G. Thorogood, Y.-B. Cheng, R. Caruso, *J. Mater. Chem.,***2012**, *22*, 17128.
7. J. Zhang, W. Peng, Z. Chen, H. Chen, L. Han, *J. Phys. Chem. C,* **2012**, *116*, 19182.
8. X. Feng, K. Shankar, M. Paulose, C. Grimes, *Angew. Chem. Int. Ed.,* **2009**, *48*, 8095.
9. M. Xu, P. Da, H. Wu, D. Zhao, G. Zheng, *Nano Let.*, **2012**, *12*, 1503.
10. R. D. Shannon, *Acta Cryst A,* **1976**, *32*, 751.
11. X. Zhang, F. Liu, Q.-L. Huang, G. Zhou, Z.-S. Wang, *J. Phys. Chem. C,* **2011**, *115*, 12665.
12. H. Kamisaka, T. Suenaga, H. Nakamura, K. Yamashita, *J. Phys. Chem. C,* **2010**, *114*, 12777.

13. K. H. Ko, Y. C. Lee, Y. J. Jung, *J. Colloid Interface Sci.,* **2005***, 283,* 482.
14. Y. M. Lee, Y. H. Kim, J. H. Lee, J. H. Park, N.-G. Park, W.-S. Choe, M. J. Ko, P. J. Yoo, *Adv. Funct. Mater.* **2011**, *21*, 1160.
15. W.-Q. Wu, Y.-F. Xu, H.-S. Rao, C.-Y. Su, D. Kuang, *Nanoscale,* **2013**, *5*, 4362.
16. E. Ramasamy, J. Lee, *Energy, Environ. Sci.,* **2011**, *4*, 2529.
17. D. Chen, F. Huang, Y.-B. Cheng, R. A. Caruso, *Adv. Mater.* **2009**, *21*, 2206.
18. X. L. Zhang, Y. Chen, A. Cant, F. Huang, Y.-B. Cheng, R. Amal, *Part. Part. Syst. Charact.* **2013**, *30*, 754.
19. S. W. Chen, J. M. Lee, S. Chiang, S. C. Haw, Y. C. Liang, K. T. Lu, C. W. Pao, J. F. Lee, M. T. Tang, J. M. Cheng, *J. Phys. Soc. Jpn.,* **2011**, *80*, 114706.
20. X. L. Zhang, F. Huang, Y. Chen, Y.-B. Cheng, R. Amal, *RSC Adv.***,** **2013,** *3*, 17003.
21. Q. Wang, S. Ito, M. Grätzel, F. Fabregat-Santiago, I. Mora-Seró, J. Bisquert, T. Bessho, H. Imai, *J. Phys. Chem. B* **2006**, *110*, 25210.
22. X. L. Zhang, Z. Zhang, F. Huang, P. Bäuerle, U. Bach, Y.-B. Cheng, *J. Mater. Chem.,* **2012**, *22*, 7005.
23. J. R. Jennings, F. Li, Q. Wang, *J. Phys. Chem. C* **2010**, *114*, 14665.
24. X. L. Zhang, Z. Zhang, D. Chen, P. Bäuerle, U. Bach, Y.-B. Cheng, *Chem. Commun.,* **2012**, *48,* 9885.
25. D. Chen, G. Xu, L. Miao, L. Chen, S. Nakao, P. Jin, *J. Appl. Phys.*, **2010,** *107*, 063707.